Supplementary Information (SI) for Journal of Materials Chemistry A.

Supporting Information

Structural origins of photocatalytic properties in Ruddlesden–Popper $Sr_{n+1}Ti_nO_{3n+1}$ (n = 1, 2) and their topochemically fluorinated phases $Sr_{n+1}Ti_nO_{(3n+1)-x}F_{2x}$ ($x \approx n$)

Shama Perween, [a]; Kevin Matthias Ries[b]; Anja Hofmann[b]; Tommi Hendrik Aalto[a]; Harol Moreno Fernández[c]; Marc Widenmeyer[d]; Robert Löser[e]; Jana Timm[b]; Guido Schmitz[e]; Petia Atanasova[f]; Jan Philipp Hofmann[c]; Oliver Clemens[a]; Roland Marschall[b]; Chengchao Zhong[g]*

[a]University of Stuttgart, Institute of Materials Science, Chemical Materials Synthesis, Heisenbergstraße 3, 70569 Stuttgart, Germany.

[b]Department of Chemistry, Chair of Physical Chemistry III University of Bayreuth, Universitätsstraße 30, 95447 Bayreuth, Germany.

[c]Technical University of Darmstadt, Department of Materials and Geosciences, Surface Science Laboratory, Peter-Grünberg-Straße 4, 64287 Darmstadt, Germany.

[d]Technical University of Darmstadt, Department of Materials and Geosciences, Research Division of Materials & Resources, Peter-Grünberg-Straße 2, 64287, Darmstadt, Germany.

[e]University of Stuttgart, Institute of Materials Science, Materials Physics, Heisenbergstraße 3, 70569 Stuttgart, Germany.

[f]University of Stuttgart, Institute of Materials Science, Bioinspired Materials, Heisenbergstraße 3, 70569 Stuttgart, Germany.

[g]Ritsumeikan University, Graduate School of Life Sciences, 1-1-1 Noji-higashi, Kusatsu, Shiga 525-8577, Japan.

Corresponding Author:

Email: shama.perween@imw.uni-stuttgart.de

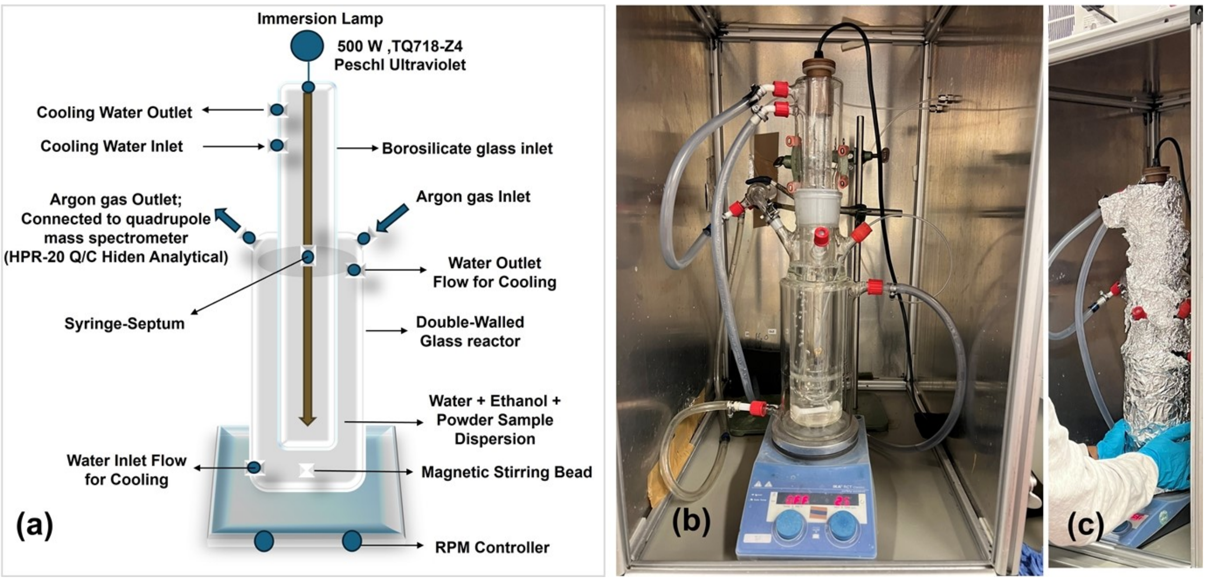

Figure S 1 (a) Schematic representation of the immersion-lamp photocatalytic reactor used for hydrogen evolution experiments. (b) Photograph of the corresponding laboratory setup (before light shielding); the schematic in (a) is drawn based on this experimental configuration. (c) Photograph of the experimental setup after full light shielding.

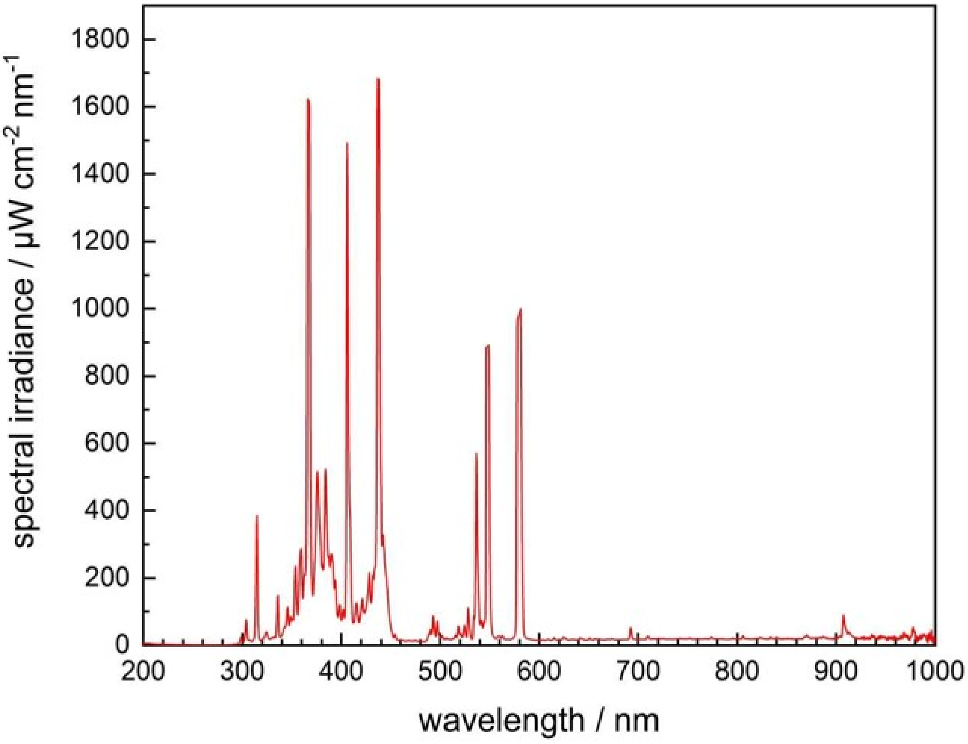

Figure S 2 Emission spectrum of the 500 W iron-doped Hg immersion lamp (TQ718-Z4, Peschl Ultraviolet) measured with a Flame spectrometer (Ocean Insight). The source shows a line (non-continuous) spectrum with discrete mercury emission peaks, in contrast to the broadband output of a Xe lamp.

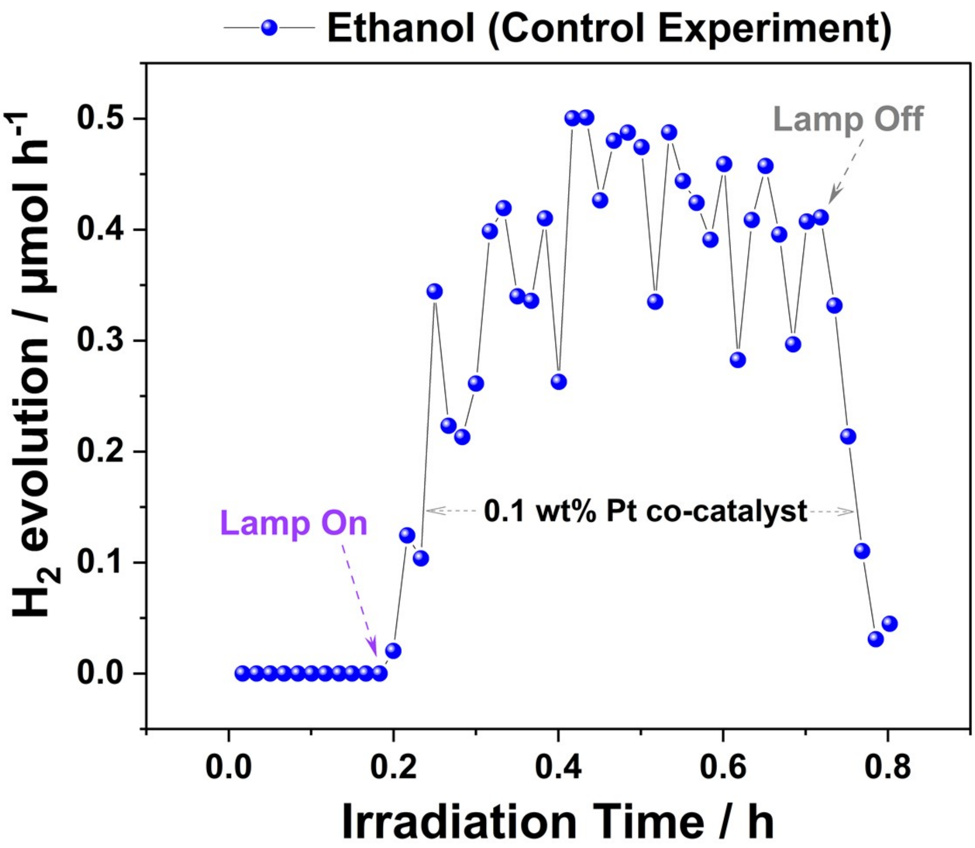

Figure S 3 Control experiment for sacrificial ethanol (EtOH) without photocatalyst but co-catalyst loading, which corresponds to only ~1/13, ~1/110, ~1/160, and ~1/5 of the hydrogen evolution achieved by Sr_2TiO_4, $Sr_2TiO_3F_2$, $Sr_3Ti_2O_7$, $Sr_3Ti_2O_5F_4$, respectively.

Table S 1 Refined lattice parameters and quantitative analysis of Sr_2TiO_4, $Sr_2TiO_3F_2$, $Sr_3Ti_2O_7$, and $Sr_3Ti_2O_5F_4$ obtained from the powder X-ray diffraction (PXRD).

Phase	**Phase Fraction [%]**	**Space Group**	**Lattice Parameters**		
			a **(Å)**	***c*** **(Å)**	**Cell Volume (Å^3)**
Sr_2TiO_4	100	*I4/mmm* (139)	3.8835(3)	12.589(2)	189.86(1)
$Sr_2TiO_3F_2$	96.59(12)	*P4/nmm* (129)	3.8048(1)	15.566(2)	225.34(2)
SrF_2	3.41(12)	$Fm\bar{3}m$ (225)	5.809(1)	5.809(1)	196.10(6)
$Sr_3Ti_2O_7$	100	*I4/mmm* (139)	3.8994(4)	20.315(2)	308.89(1)
$Sr_3Ti_2O_5F_4$	100	*I4/mmm* (139)	3.909(2)	23.374(2)	357.19(4)

Table S 2 Refined lattice parameters and quantitative phase analysis of Sr_2TiO_4, $Sr_2TiO_3F_2$, $Sr_3Ti_2O_7$, and $Sr_3Ti_2O_5F_4$ compiled from literature values,[1, 2] to enable comparison with the present work in **Table S 1**.

Phase	**Phase Fraction [%]**	**Space Group**	**Lattice Parameters**		
			***a* (Å)**	***c* (Å)**	**Cell Volume (Å^3)**
Sr_2TiO_4	100	*I4/mmm* (139)	3.885(1)	12.59(1)	190.07(1)
$Sr_2TiO_3F_2$	95.7(1)	*P4/nmm* (129)	3.804 (1)	15.51(1)	224.46(9)
SrF_2	4.4(1)	$Fm\bar{3}m$ (225)			
$Sr_3Ti_2O_7$	100	*I4/mmm* (139)	3.899(2)	20.31(1)	308.78(3)
$Sr_3Ti_2O_5F_4$	87.79(18)	*I4/mmm* (139)	3.906(2)	23.37(2)	357.451(3)
$SrTiO_3$	7.09(8)	$Pm\bar{3}m$ (221)	3.908(2)	3.908(2)	59.6(3)
SrF_2	5.12(17)	$Fm\bar{3}m$ (225)	5.813(1)	5.813(1)	196.4(3)

Table S 3 Crystallographic refinement quality indicators for Sr_2TiO_4, $Sr_2TiO_3F_2$, $Sr_3Ti_2O_7$, and $Sr_3Ti_2O_5F_4$ obtained from Rietveld refinement of PXRD data at ambient temperature and pressure for the present work.

Compound	**Residual of least square refinement (R_p) [%]**	**weighted-profile R-factor (R_{wp}) [%]**	**weighted-profile R-factor (R_{exp}) [%]**	**Goodness of Fit (X^2)**
Sr_2TiO_4	4.43	6.07	4.98	1.22
$Sr_2TiO_3F_2$	7.69	9.72	7.11	1.37
$Sr_3Ti_2O_7$	9.21	12.36	2.82	4.39
$Sr_3Ti_2O_5F_4$	7.39	9.62	6.88	1.40

Table S 4 Refined bond distances of *n* = 1 phases (Sr_2TiO_4 and $Sr_2TiO_3F_2$) from PXRD, along with selected literature values[1] from combined PXRD/neutron diffraction for comparison.

Bond (site)	**Bond distance (Å)**		
	Sr_2TiO_4	**$Sr_2TiO_3F_2$**	
	Present Work	**Present Work**	**Literature**
Sr1−*X*1 (equatorial)	2.676(9)	2.816(5)	--
Sr1−*X*2 (apical)	2.479(3)	2.431(9)	--
Sr1−*X*4 (Interstitial)	--	2.509(3)	--
Sr2−*X*1 (equatorial)	--	--	--
Sr2−*X*2 (apical)	--	2.784(1)	--
Ti1−*X*1 (equatorial)	1.942(4)	1.951(1) (4x)	1.93 (4x)
Ti1−*X*2 (apical−short)	1.974(3)	1.701(4) (1x)	1.81 (1x)
Ti1−*X*3 (apical−long)	--	2.81(6) (1x)	2.63 (1x)

Table S 5 Refined bond distances of *n* = 2 phases ($Sr_3Ti_2O_7$ and $Sr_3Ti_2O_5F_4$) from PXRD. Anion sites are denoted as *X*1 (equatorial), *X*2 (apical−central), *X*3 (apical−terminal), and *X*4 (Interstitial), along with selected literature values[2] from combined PXRD/neutron diffraction for comparison.

Bond	**Bond distance (Å)**			
	$Sr_3Ti_2O_7$		**$Sr_3Ti_2O_5F_4$**	
	Present Work	**Literature**	**Present Work**	**Literature**
Sr1−*X*1	2.75(3) (8x)	2.755(3) (8x)	2.77(3) (8x)	2.750(2) (8x)
Sr1−*X*2	2.76(2) (4x)	2.7572(1) (4x)	2.81(2) (4x)	2.7723(3) (4x)
Sr2−*X*1	2.67(3) (4x)	2.674(3) (4x)	3.13(2) (4x)	3.130(2) (4x)
Sr2−*X*3	2.76(2) (4x)	2.7593(2) (4x)	2.81(5) (4x)	2.8105(6) (4x)
Sr2−*X*4	--	--	2.47(6) (4x)	2.4666(8) (4x)
Ti1−*X*1	1.950(2) (4x)	1.9501(1) (4x)	1.96(5) (4x)	1.9608(4) (4x)
Ti1−*X*2	1.742(8) (1x)	1.989(2) (1x)	1.89(9) (1x)	1.886(2) (1x)
Ti1−*X*3	--	1.897(5) (1x)	2.01(4) (4x)	2.020(3) (4x)

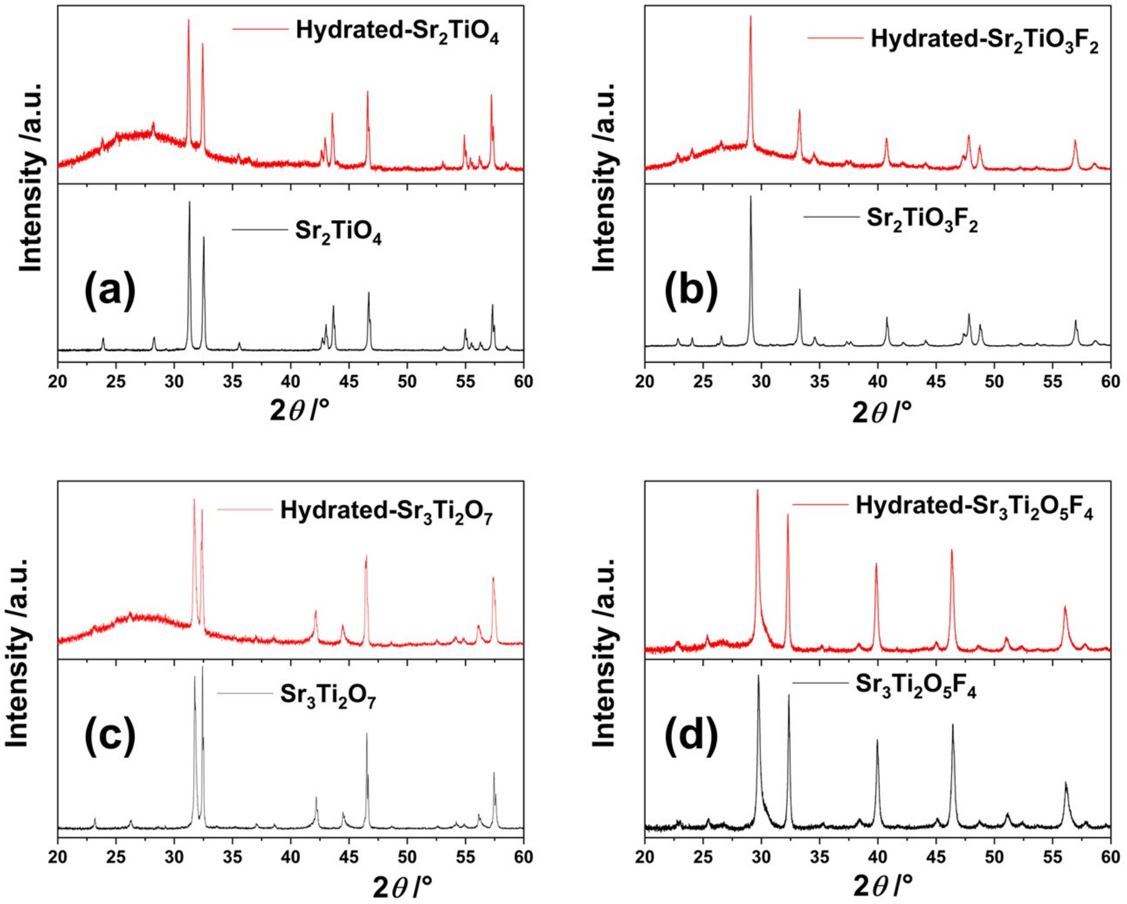

Figure S 4 PXRD patterns of hydrated phases obtained after soaking compounds in deionized water (DI-H_2O) for 24 h under ambient conditions: (a) Sr_2TiO_4, (b) $Sr_2TiO_3F_2$, (c) $Sr_3Ti_2O_7$, and (d) $Sr_3Ti_2O_5F_4$. Samples were measured by drop-casting aqueous suspensions onto the XRD substrate, with the visible broad hump at lower 2θ values arising from the residual water contribution.

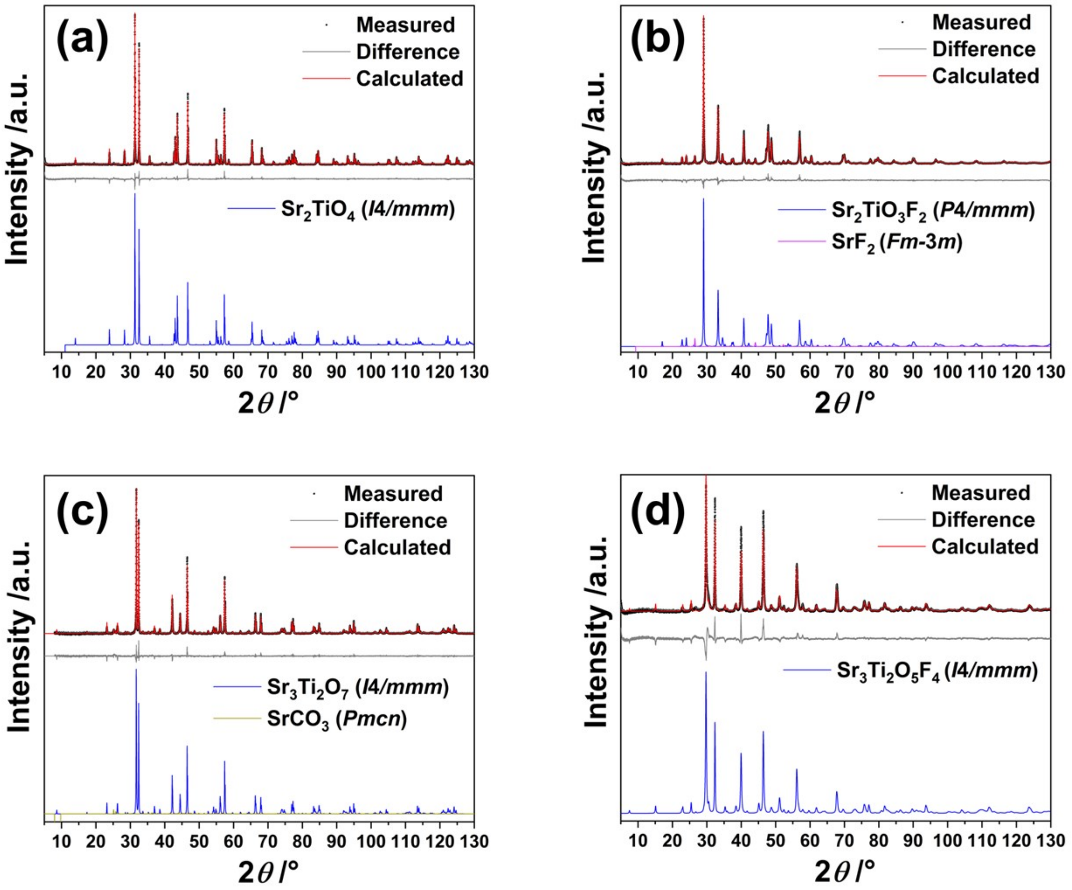

Figure S 5 Rietveld refinements of PXRD data from aged samples (~1.5 years): (a) Sr_2TiO_4, (b) $Sr_2TiO_3F_2$, (c) $Sr_3Ti_2O_7$, and (d) $Sr_3Ti_2O_5F_4$. An additional trace amount of $SrCO_3$ (wt% 3.1(1)) is observed in the *n* = 2 oxide, $Sr_3Ti_2O_7$.

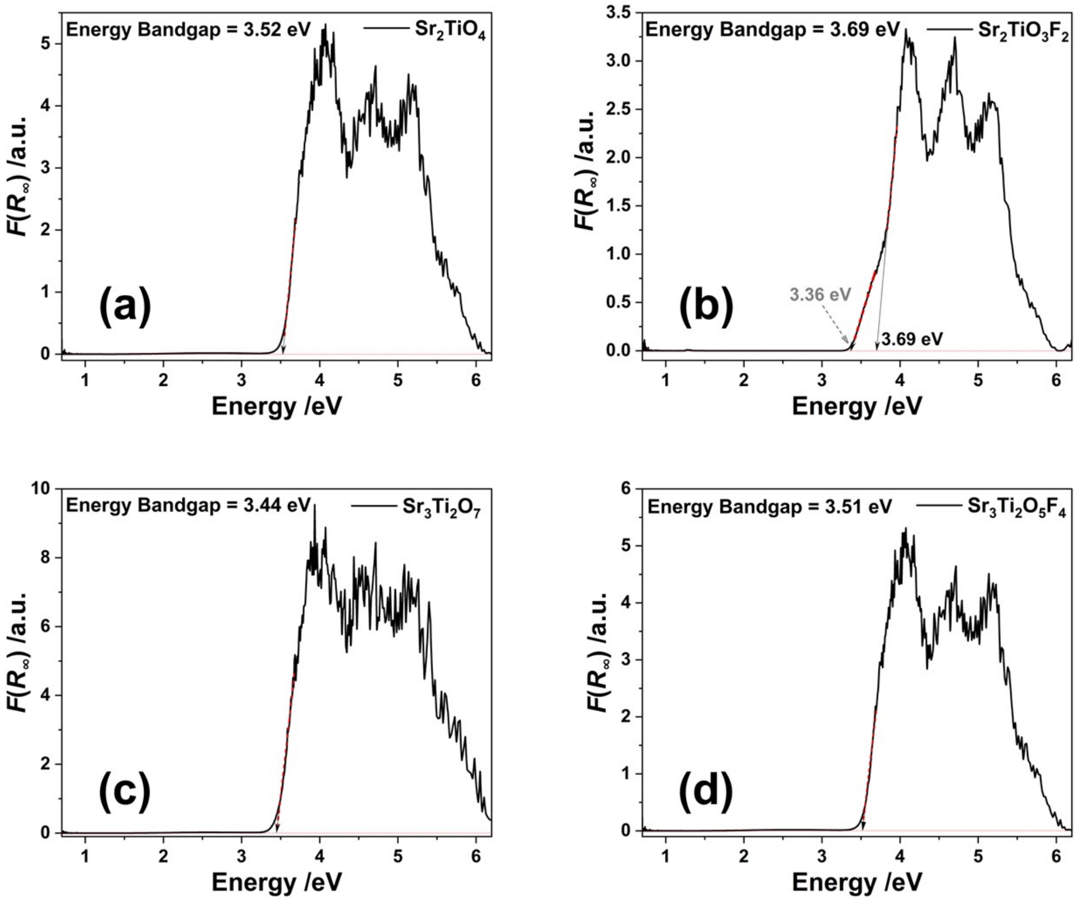

Figure S 6 Ultra-violet (UV)−visible Kubelka−Munk (K−M) energy plots of oxide and their corresponding oxyfluorides: (a) Sr_2TiO_4, (b) $Sr_2TiO_3F_2$, (c) $Sr_3Ti_2O_7$, and (d) $Sr_3Ti_2O_5F_4$.

Table S 6 Elemental ionization energies (IE) and electron affinities (EA) with the resulting absolute Mulliken electronegativities (χ_i, eV) used in the Butler–Ginley,[3-9] together with the formula-unit stoichiometry and total atom count for Sr_2TiO_4, $Sr_2TiO_3F_2$, $Sr_3Ti_2O_7$, and $Sr_3Ti_2O_5F_4$; for the comparison, the values for RP-type indate,[10] $LaBaInO_4$*, and $LaBaInO_3F_2$*, are also included.

Element	Ionization Energy (IE), eV	Electron Affinity (EA), eV	Mulliken electronegativity (absolute), χ_i (eV)	Compound	Stoichiometry	Total number of atoms
Sr	5.695	0.048	2.87	Sr_2TiO_4	(Sr_2TiO_4: Sr:2, Ti:1, O:4, F:0):	7
Ti	6.828	0.076	3.45	$Sr_2TiO_3F_2$	($Sr_2TiO_3F_2$: Sr:2, Ti:1, O:3, F:2):	8
O	13.618	1.462	7.54	$Sr_3Ti_2O_7$	($Sr_3Ti_2O_7$: Sr:3, Ti:2, O:7, F:0):	12
F	17.423	3.401	10.41	$Sr_3Ti_2O_5F_4$	($Sr_3Ti_2O_5F_4$: Sr:3, Ti:2, O:5, F:4):	14
***La**	5.577	0.558	3.07	*$LaBaInO_4$	($LaBaInO_4$: La:1, Ba:1, In:1, O:4, F:0):	7
***Ba**	5.212	0.145	2.68	*$LaBaInO_3F_2$	($LaBaInO_3F_2$: La:1, Ba:1, In:1, O:3, F:2):	8
***In**	5.786	0.384	3.09	--	--	--

Table S 7 Semi-empirical band-edge positions vs NHE estimated by the Butler–Ginley electronegativity method using UV–Vis–DRS band gaps. Values are given vs NHE; reference RHE at *p*H 7.0 values are also listed. For cross-system comparison, the same analysis is included for the RP-type indates[10] $LaBaInO_4$*, and $LaBaInO_3F_2$* from the literature.

Compound	**E_g (UV-Vis DRS)**	$\bar{\chi}$	**E_{CB} vs NHE**	**E_{VB} vs NHE**	**E_{CB} vs RHE**	**E_{VB} vs RHE**
	(eV)					
Sr_2TiO_4	3.52	5.12	-1.14	+2.38	-0.728	+2.79
$Sr_2TiO_3F_2$	3.36	5.82	-0.36	+3.00	+0.057	+3.42
$Sr_3Ti_2O_7$	3.44	5.20	-1.02	+2.42	-0.606	+2.83
$Sr_3Ti_2O_5F_4$	3.51	6.01	-0.24	+3.27	+0.172	+3.68
*$LaBaInO_4$	1.80	5.03	-0.37	+1.43	+0.048	+1.85
*$LaBaInO_3F_2$	3.30	5.74	-0.41	+2.89	+0.003	+3.30
	1.90	5.74	+0.29	+2.19	+0.703	+2.60

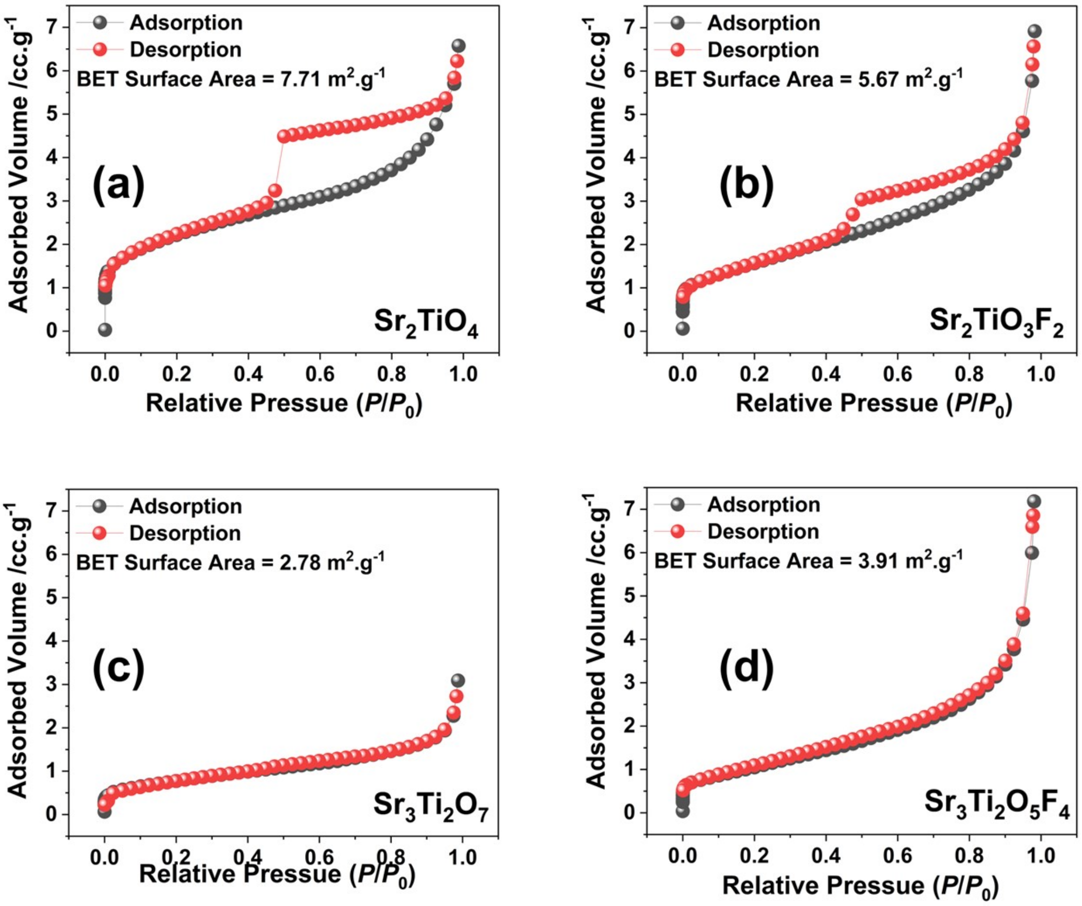

Figure S 7 N_2 adsorption-desorption isotherms and BET surface areas: (a) Sr_2TiO_4, (b) $Sr_2TiO_3F_2$, (c) $Sr_3Ti_2O_7$, and (d) and $Sr_3Ti_2O_5F_4$.

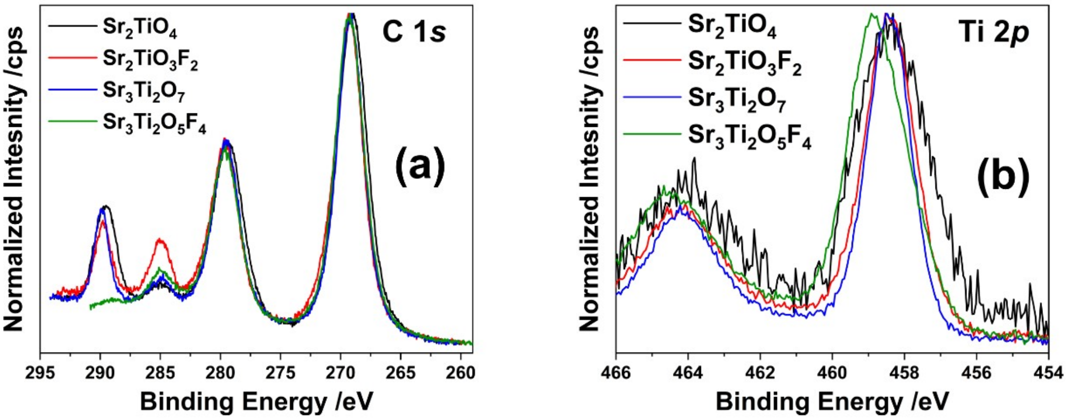

Figure S 8 X-ray photoelectron spectroscopy (XPS) spectra of the compounds showing (a) C 1*s* used as a reference for calibration, and (b) an enlarged view of Ti 2*p* region highlighting the relative chemical shift for $Sr_3Ti_2O_5F_4$.

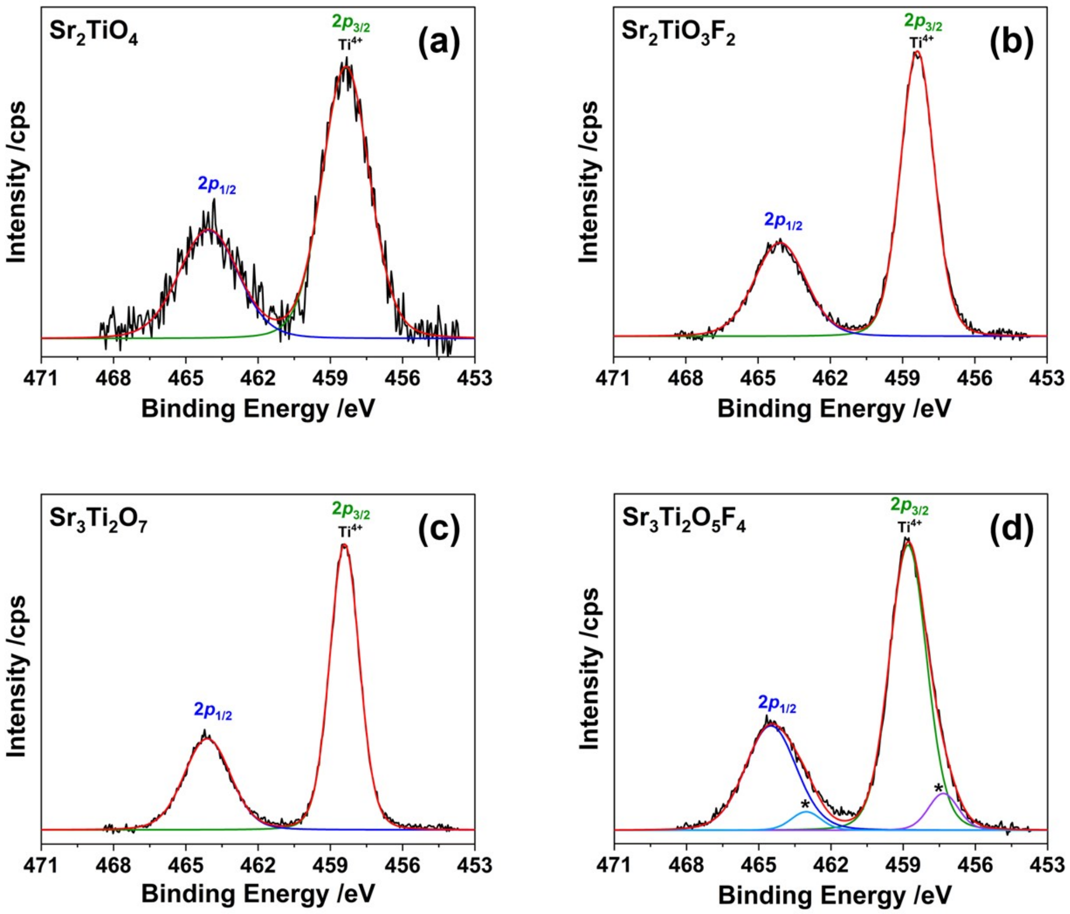

Figure S 9 XPS Ti 2*p* spectra of the compounds (a) Sr_2TiO_4, (b) $Sr_2TiO_3F_2$, (c) $Sr_3Ti_2O_7$, and (d) $Sr_3Ti_2O_5F_4$. The asterisk (*) marks the minor Ti^{4+} component associated with non-uniform O/F coordination environment.

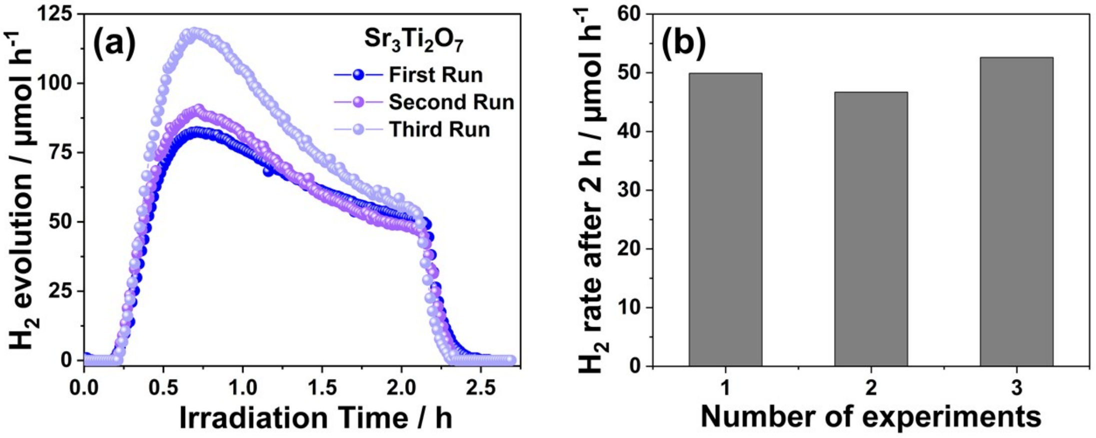

Figure S 10 Reproducibility of photocatalytic hydrogen evolution for $Sr_3Ti_2O_7$ measured in three independent runs under identical experimental conditions performed at different times. All runs show similar hydrogen evolution behavior and converge to a comparable steady-state activity after 2 h of irradiation.

Table S 8 The optical energy bandgaps (Kubelka−Munk plots), BET surface areas, and photocatalytic hydrogen (H_2) evolution mole counts of Sr_2TiO_4, $Sr_2TiO_3F_2$, $Sr_3Ti_2O_7$, and $Sr_3Ti_2O_5F_4$ under UV−light irradiation.

Compound	**Bandgap Energy (eV)**	**BET Surface Area (m^2 g^{-1})**	**H_2 evolution (μmol h^{-1})**		**Relative comparison with respect to oxyfluorides compounds**
			At initial 0.5 h light irradiation	**After 2 h light irradiation**	
Sr_2TiO_4 (*n* = 1)	3.52	7.71	8.60	8.02	~6.3-fold higher initially; ~5-fold higher after 2 h
Sr_2TiO_3F (*n* = 1)	3.36 / 3.69	5.67	54.64	40.05	
$Sr_3Ti_2O_7$ (*n* = 2)	3.44	2.78	82.44	51.83	~30-fold higher initially; ~26-fold higher after 2 h
$Sr_3Ti_2O_5F_4$ (*n* = 2)	3.51	3.91	2.74	1.99	

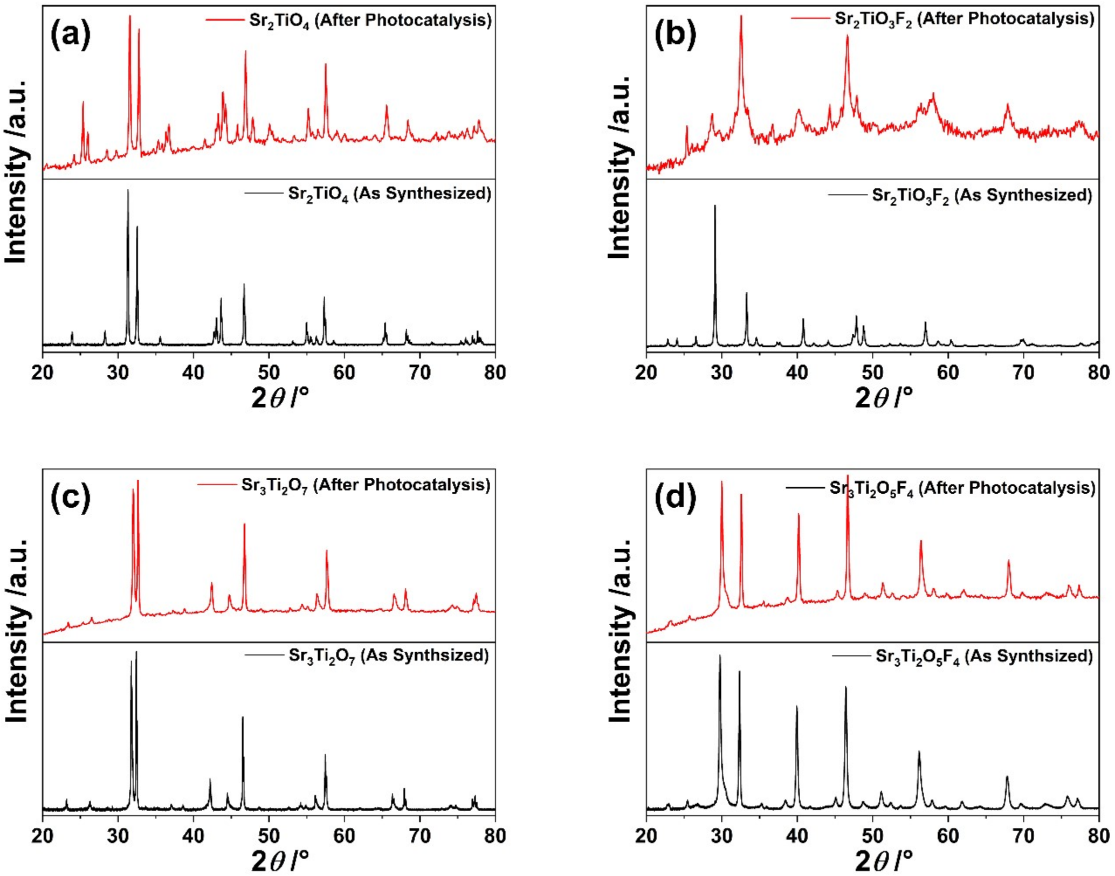

Figure S 11 PXRD patterns of RP oxides and oxyfluorides measured before (as synthesized) and after photocatalytic hydrogen evolution: (a) Sr_2TiO_4, (b) $Sr_2TiO_3F_2$, (c) $Sr_3Ti_2O_7$, and (d) $Sr_3Ti_2O_5F_4$. For the *n* = 1 oxide and oxyfluoride phases, changes in relative peak intensities and the appearance of additional reflections after photocatalysis indicate partial structural degradation under the applied reaction conditions. In contrast, the *n* = 2 oxide and oxyfluoride phases retain their characteristic diffraction patterns after photocatalysis, indicating higher structural stability of the double-layered Ruddlesden−Popper framework under aqueous photocatalytic conditions.

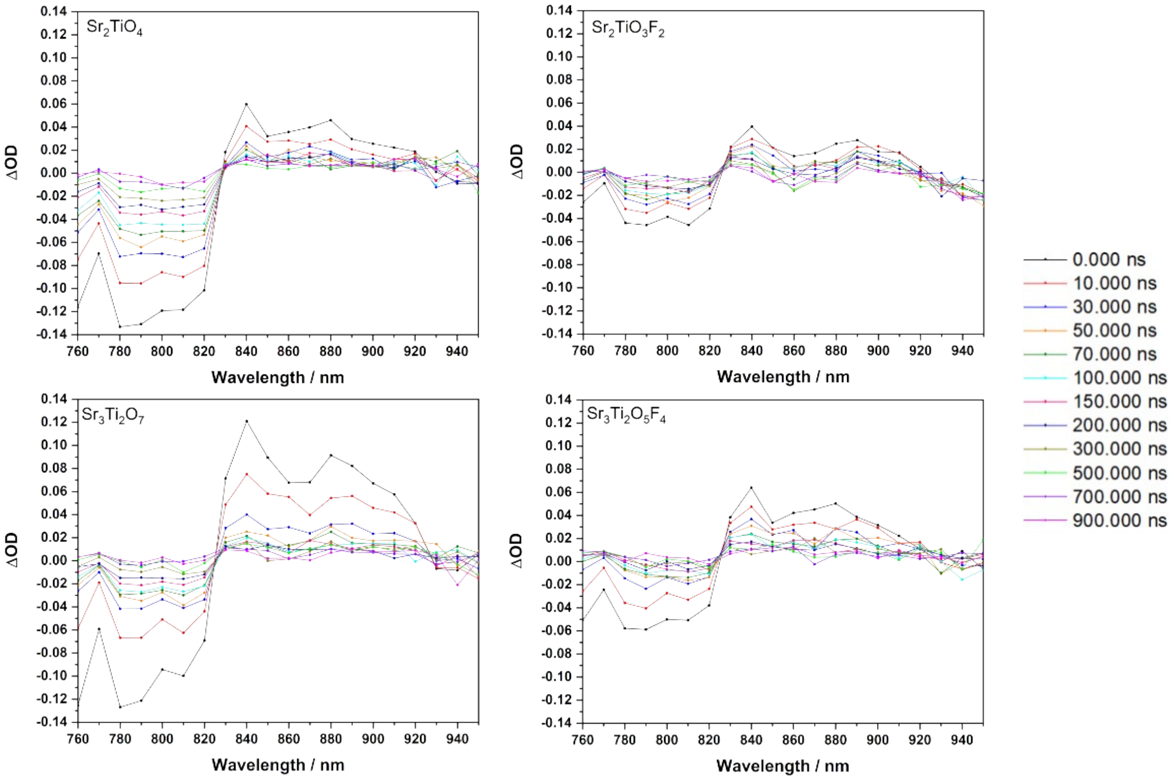

Figure S 12 TAS maps of the samples Sr_2TiO_4, $Sr_2TiO_3F_2$, $Sr_3Ti_2O_7$ and $Sr_3Ti_2O_5F_4$ with λ_{Exc}=355 nm.

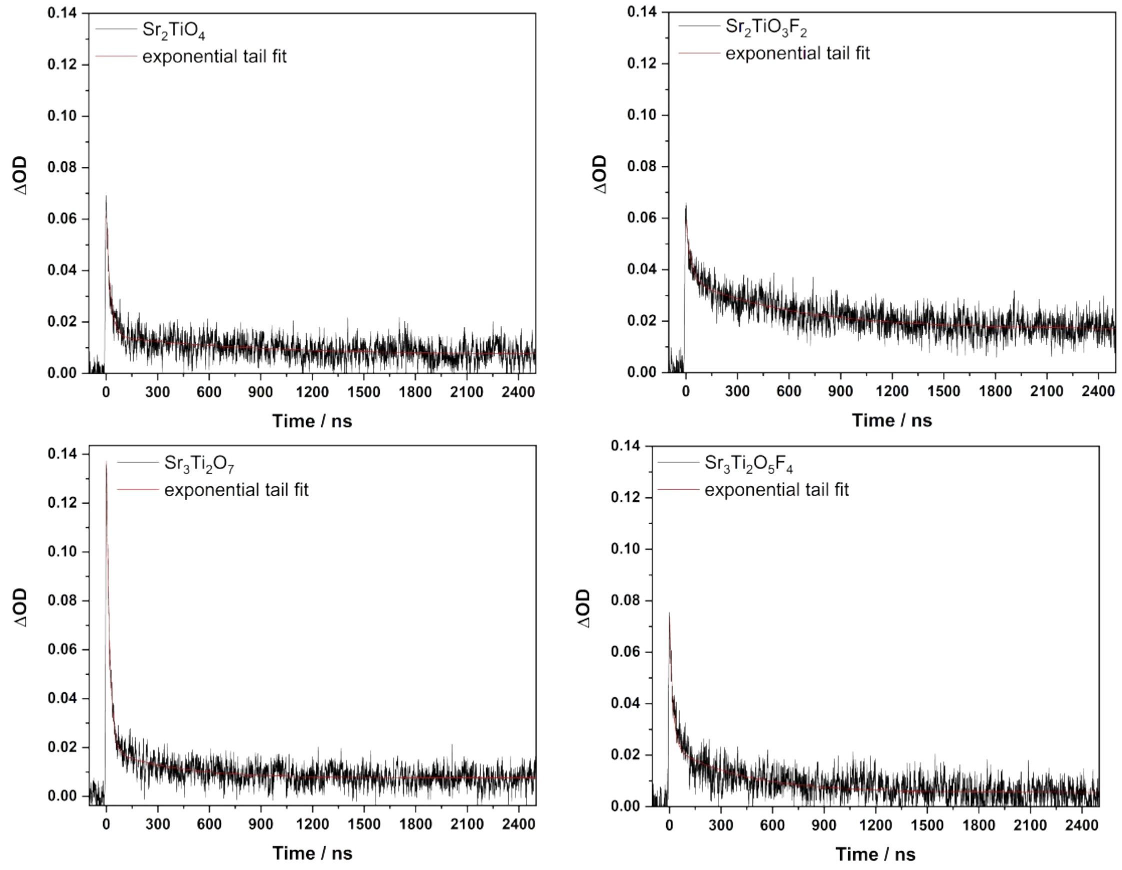

Figure S 13 TAS decays of the samples Sr$_2$TiO$_4$, Sr$_2$TiO$_3$F$_2$, Sr$_3$Ti$_2$O$_7$ and Sr$_3$Ti$_2$O$_5$F$_4$ with λ_{Exc}=355 nm and λ_{probe}=840 nm.

Table S 9 Lifetimes of the photogenerated electrons of the samples Sr$_2$TiO$_4$, Sr$_2$TiO$_3$F$_2$, Sr$_3$Ti$_2$O$_7$ and Sr$_3$Ti$_2$O$_5$F$_4$ with λ_{Exc} = 355 nm and λ_{probe} = 840 nm. The results were achieved via biexponential fitting.

Compound	**840 nm**
Sr$_2$TiO$_4$	23.6 ns / 823.9 ns
Sr$_2$TiO$_3$F$_2$	28.5 ns / 624.0 ns
Sr$_3$Ti$_2$O$_7$	18.6 ns / 379.1 ns
Sr$_3$Ti$_2$O$_5$F$_4$	18.6 ns / 421.7 ns

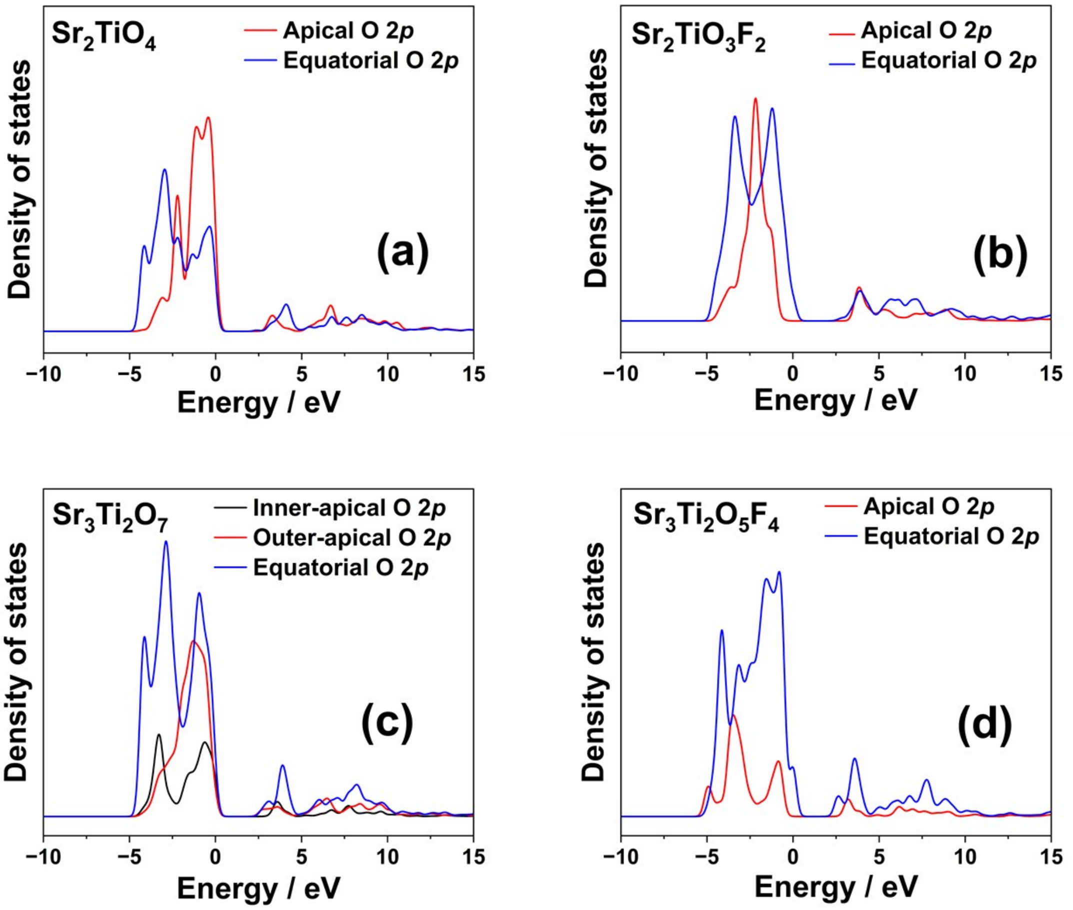

Figure S 14 Partial density of states (PDOS) of the O 2*p* orbitals for (a) Sr_2TiO_4, (b) $Sr_2TiO_3F_2$, (c) $Sr_3Ti_2O_7$, and (d) $Sr_3Ti_2O_5F_4$, highlighting the differences between apical and equatorial oxygen contributions. For $Sr_3Ti_2O_7$, the inner- and outer-apical O 2*p* states are shown separately.

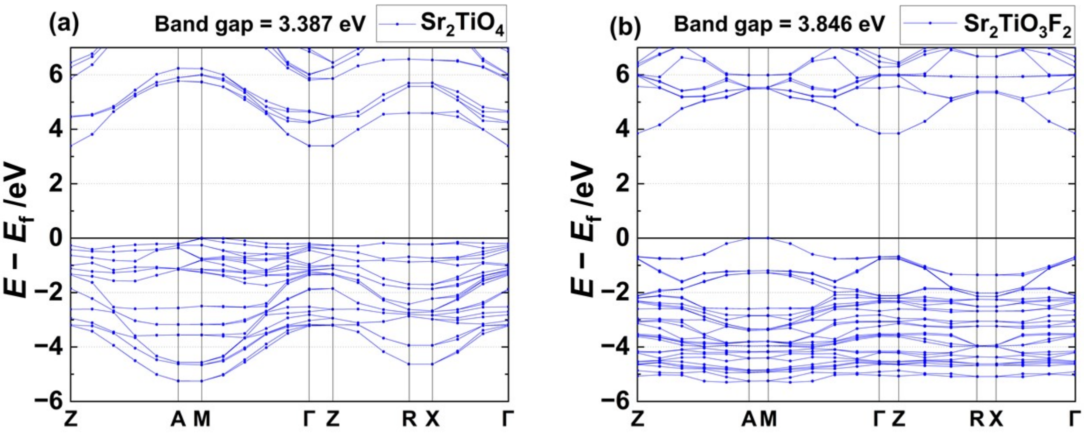

Figure S 15 Heyd−Scuseria−Ernzerhof (HSE06) hybrid-functional electronic band structures of (a) Sr_2TiO_4 and (b) $Sr_2TiO_3F_2$. The calculated band gaps are 3.387 eV and 3.846 eV, respectively. While the absolute bandgaps are larger than those obtained using the PBE functional, the relative bandgaps widening upon fluorination is preserved. The Fermi level is set to 0 eV.

REFERENCES

(1) Wissel, K.; Dasgupta, S.; Benes, A.; Schoch, R.; Bauer, M.; Witte, R.; Fortes, A. D.; Erdem, E.; Rohrer, J.; Clemens, O. Developing intercalation based anode materials for fluoride-ion batteries: topochemical reduction of $Sr_2TiO_3F_2$ via a hydride based defluorination process. *Journal of Materials Chemistry A* **2018**, *6*, 22013–22026. DOI: 10.1039/c8ta01012a.

(2) Wissel, K.; Vogel, T.; Dasgupta, S.; Fortes, A. D.; Slater, P. R.; Clemens, O. Topochemical Fluorination of $n = 2$ Ruddlesden−Popper Type $Sr_3Ti_2O_7$ to $Sr_3Ti_2O_5F_4$ and Its Reductive Defluorination. *Inorganic Chemistry* **2020**, *59*, 1153−1163. DOI: 10.1021/acs.inorgchem.9b02783.

(3) Walsh, A.; Butler, K. T. Prediction of Electron Energies in Metal Oxides. *Accounts of Chemical Research* **2014**, *47* (2), 364–372. DOI: 10.1021/ar400115x.

(4) Butler, M. A.; Ginley, D. S. Prediction of Flatband Potentials at Semiconductor-Electrolyte Interfaces from Atomic Electronegativities. *Journal of The Electrochemical Society* **1978**, *125* (2), 228–232. DOI: 10.1149/1.2131419.

(5) Halouani, F. E.; Deschanvres, A. Interfaces semi-conducteur-electrolyte: Correlations entre le potentiel de bande plate et les echelles d'electronegativite. *Materials Research Bulletin* **1982**, *17* (8), 1045-1052. DOI: 10.1016/0025-5408(82)90130-1.

(6) Arthur H. Nethercot, J. Prediction of Fermi Energies and Photoelectric Thresholds Based on Electronegativity Concepts. *Physical Review Letters* **1974**, *33*, 1088. DOI: 10.1103/PhysRevLett.33.1088.

(7) NIST Atomic Spectra Database (ver. 5.12), [Online]. https://physics.nist.gov/asd (accessed 22 September 2025).

(8) Russell, D.; III, J. *NIST Computational Chemistry Comparison and Benchmark Database, NIST Standard Reference Database Number 101.* 2022. http://cccbdb.nist.gov/ (accessed 22 September 2025).

(9) Mulliken, R. S. A New Electroaffinity Scale; Together with Data on Valence States and on Valence Ionization Potentials and Electron Affinities. *The Journal of Chemical Physics* **1934**, *2*, 782–793. DOI: 10.1063/1.1749394.

(10) Perween, S.; Wissel, K.; Dallos, Z.; Weiss, M.; Ikeda, Y.; Vasala, S.; Strobel, S.; Schützendübe, P.; Jeschenko, P. M.; Kolb, U.; et al. Topochemical Fluorination of $LaBaInO_4$ to $LaBaInO_3F_2$, Their Optical Characterization, and Photocatalytic Activities for Hydrogen Evolution. *Inorganic Chemistry* **2023**, *62*, 16329−16342. DOI: 10.1021/acs.inorgchem.3c01682.